Supporting Information

1. Experimental Section

1.1 Chemicals

$FeCl_3 \cdot 6H_2O$ (A.R., 99.0%) , $CoCl_2 \cdot 6H_2O$(A.R., 99.0%), $Cr(NO_3)_3 \cdot 9H_2O$ (A.R., 99.0%) and $CO(NH_2)_2$ (A.R., 99.0%) were purchased from Titan. Nickel Foam (NF) purchased from Suzhou Kesheng and Metal Materials.

All reagents can be used without further purification.

1.2 Determination of Active Chlorine

The concentration of active chlorine in the electrolyte was measured using a UV-vis spectrophotometer based on the KI method.

Using Cr-FeCo LDH/NiS_x as the working electrode, continuous electrolysis was conducted for 100 hours at a constant current density (100 mA cm^{-2}) in both 1 M KOH + 0.5 M NaCl and 1 M KOH + Seawater electrolytes. Following electrolysis, 2 ml samples of both untreated and electrolyzed solutions were taken. Each sample was sequentially mixed with 2 ml of 0.5 M KI solution and 1 ml of 0.2 M H_2SO_4 solution for pH adjustment, allowing the mixture to react for one minute. Subsequently, the UV-visible spectra of each sample were measured within the 200-400 nm range.

2. DFT Calculations

Density functional theory (DFT) based first-principles calculations are conducted using projected augmented wave (PAW) method implemented in the Vienna ab initio simulation package (VASP). The Kohn-Sham one-electron states are expanded using the plane-wave basis set with a kinetic energy cutoff of 450 eV. The generalized gradient approximation (GGA) with Perdew-Burke-Ernzerhof (PBE) was applied to address the nonlocal exchange correlation energy. A sufficiently large vacuum region of 15 Å in the vertical that was used for the systems to investigate the mechanism of surface reactions. The Brillouin-zone integration is carried out using the Monkhorst-Pack sampling method with a density of 3×3×1 for optimizations. During the geometry optimizations, it was allowed to relax until the maximum magnitude of the force acting on the atoms is smaller than 0.02 eV/Å, and the total energy convergence

criterion is set to 1 × 10^{-4} eV. The calculation of the Gibbs free energy of the intermediates followed the Nørskov method. The adsorption energy (E_{ads}) of the activated molecules on electrocatalyst surfaces was defined as: $\Delta E_{ads} = E_{ad/sub} - E_{ad} - E_{sub}$. The $E_{ad/sub}$, E_{ad}, and E_{sub} represent the energies of the substrate with adsorbate species, the adsorbate species and the substrate, respectively. For each step, Gibbs free energy(ΔG) change was calculated as: $\Delta G = \Delta E_{ads} + \Delta ZPE - T\Delta S$. The ΔZPE, ΔS and T represent zero-point energy change, entropy change between the adsorbate species and the substrate, and the temperature (The temperature is set to 298.15 K in this work), respectively. ΔZPE can be calculated by additional vibrational frequency analysis.

The amorphous primitive cell phase was generated by ab initio molecular dynamics (AIMD) simulations: the crystalline unit cell was expanded into a 3 × 3 × 3 supercell, heated to 2500 K, and subsequently quenched to 300 K over a total simulation time of 12 ps under the isothermal–isobaric (NPT) ensemble. The resulting amorphous structure was further optimized by full ionic relaxation. Given the large lateral dimensions of the heterostructure supercell, Brillouin zone integration was carried out on a 2 × 3 × 1 Γ-centered Monkhorst–Pack k-point grid. The self-consistent field cycle was converged to a total energy tolerance of 10^{-6} eV, and ionic positions were relaxed until all residual Hellmann–Feynman forces fell below 0.03 eV $Å^{-1}$. Gaussian smearing with a width of σ = 0.05 eV was applied to facilitate Fermi-level integration.

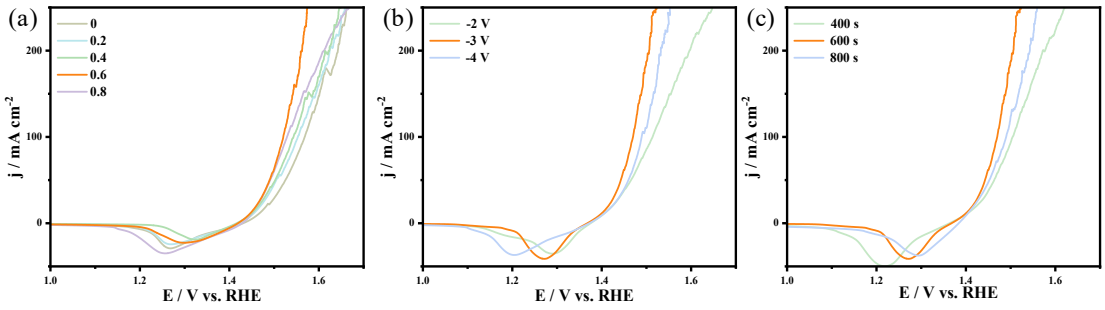

Fig. S1 LSV of (a) Cr-FeCo LDH with different Cr doping ratios, (b) Cr-FeCo LDH/NiS_x with different electrodeposition voltages, (c) Cr-FeCo LDH/NiS_x with different electrodeposition times.

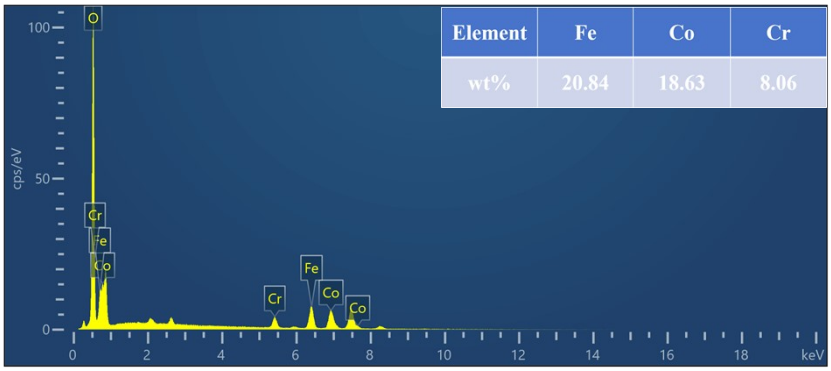

Fig. S2 Quantifying the elements contents in Cr-CoFe-LDH/NF by EDS.

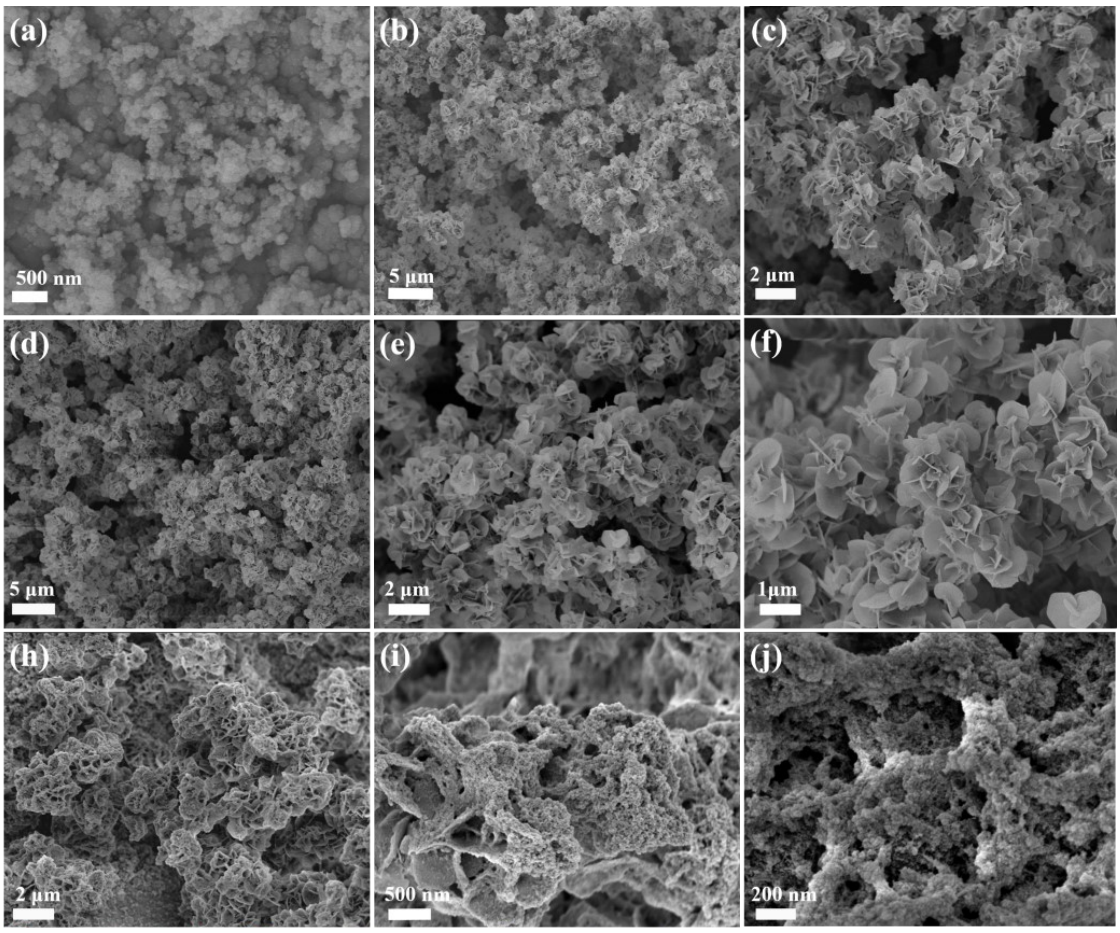

Fig. S3 SEM images of (a) NiS_x, (b-c) FeCo LDH, (d-f) Cr-FeCo LDH, (h-j) Cr-FeCo LDH/NiS_x .

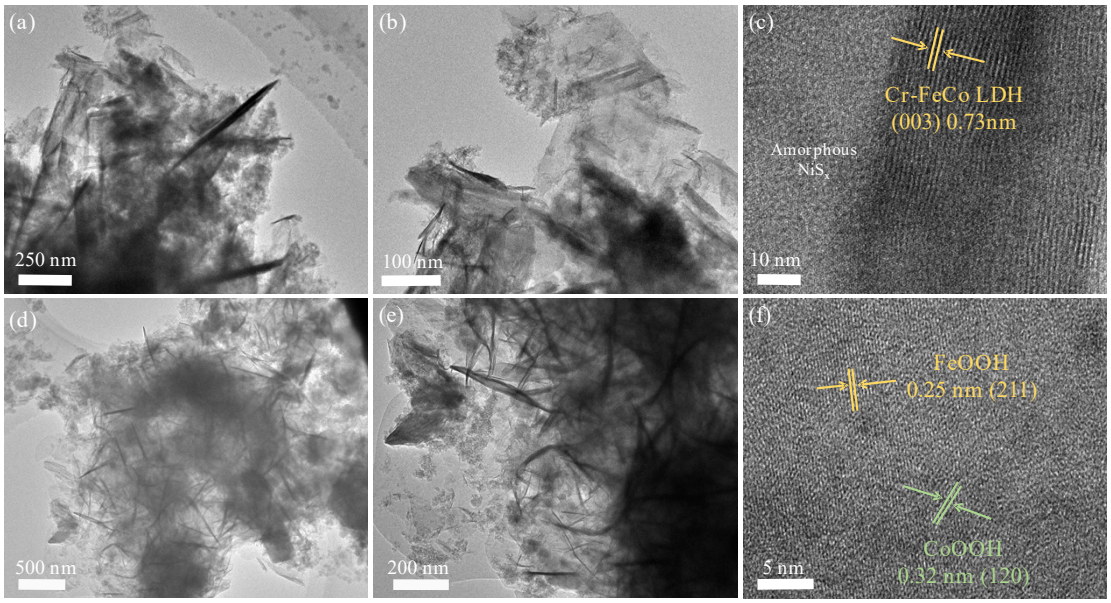

Fig. S4 TEM and HRTEM images of Cr-FeCo LDH/NiS_x (a-c) before OER, (d-f) after OER.

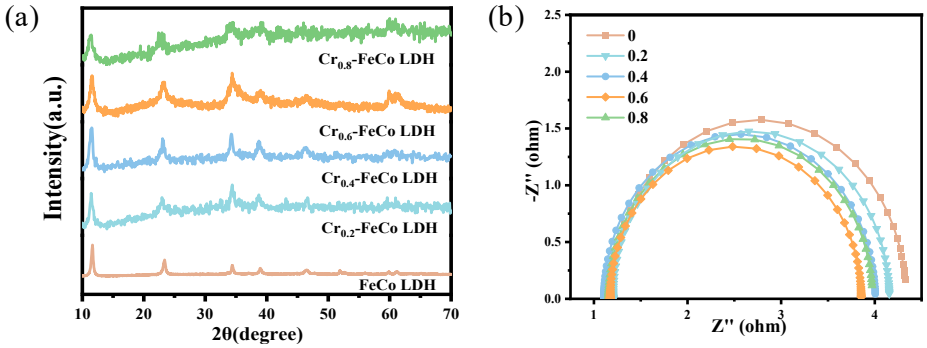

Fig. S5 (a-b) XRD patterns and EIS spectra of Cr-FeCo LDH/NiS_x with different Cr doping amounts.

As Cr doping increases, XRD peaks broaden due to microstrain and grain refinement from ionic radius differences (Fig.S5a). At the optimal 0.6 mmol doping, good crystallinity is maintained. Moderate lattice distortion regulates the electronic structure and drives surface reconstruction, while excessive doping disrupts long-range order, impairs conduction, and hinders reconstruction.

The reconstruction process involves proton-electron coupled transfer. As shown in Fig. S5b, at the optimum concentration, the sample exhibits minimal charge transfer resistance (Rct) and the fastest charge transport, effectively lowering the reconstruction energy barrier. Conversely, concentrations that are either too low or too high increase Rct, resulting in sluggish charge transfer and creating a kinetic

bottleneck that subsequently impairs catalytic activity and reconstruction efficiency.

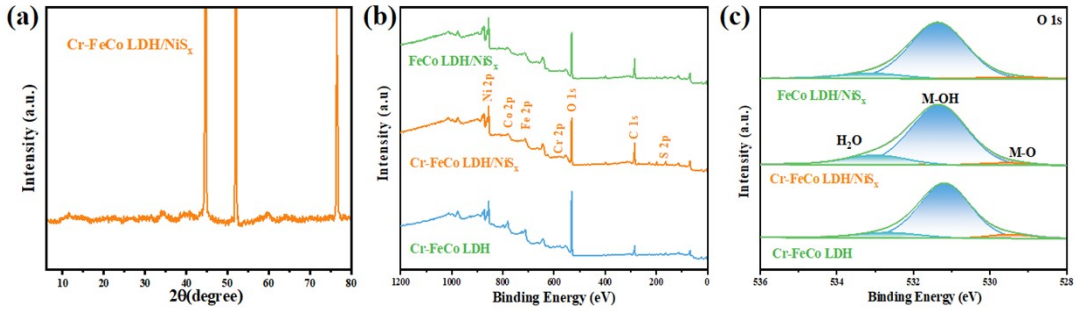

Fig. S6 (a) XRD patterns of Cr-FeCo LDH/NiS_x (b) XPS survey spectra and O 1s XPS spectra of FeCo LDH , FeCo LDH/NiS_x and Cr-FeCo LDH/NiS_x.

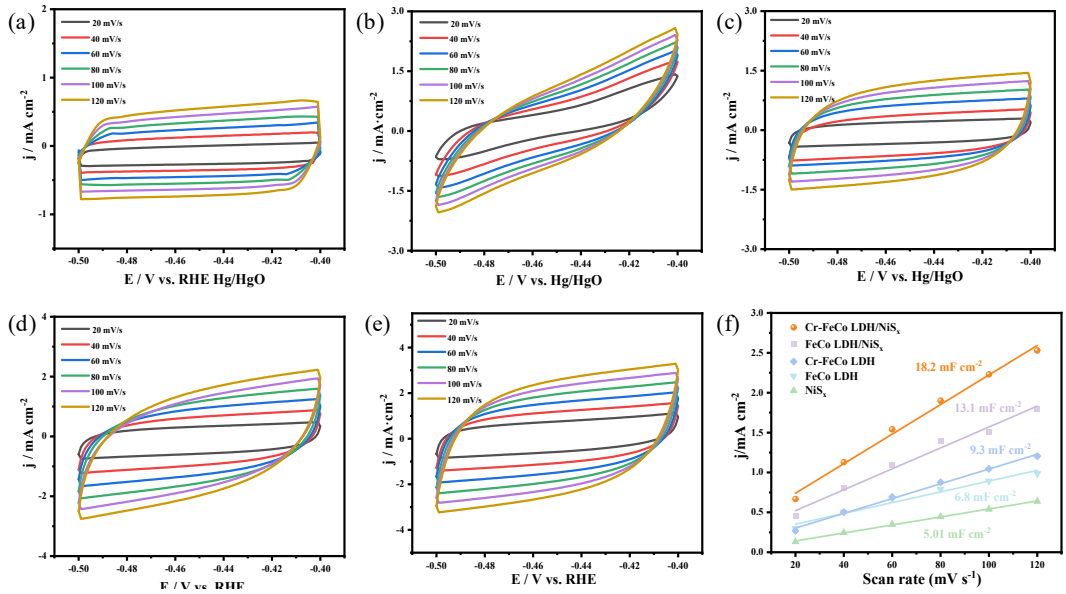

Fig. S7 Cyclic voltammetry curves of (a) NiS_x, (b) FeCo LDH, (c) Cr-FeCo LDH, (d) FeCo LDH/NiS_x , (e) Cr-FeCo LDH/NiS_x, (f) Calculated C_{dl} of the catalysts .

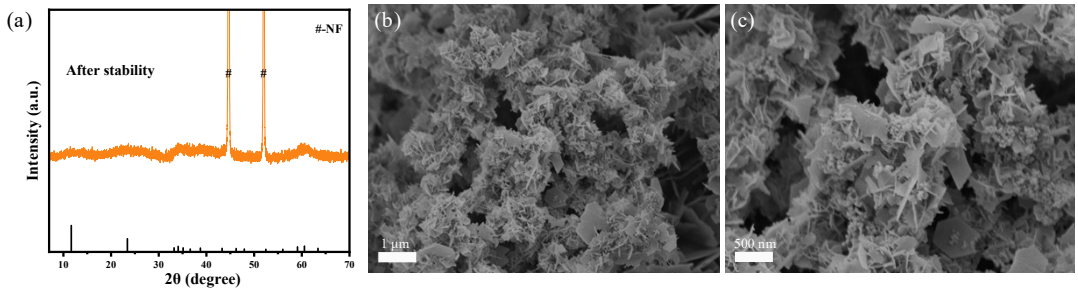

Fig. S8 (a) XRD patterns of Cr-FeCo LDH/NiS_x after stability testing, (b-c) SEM images of Cr-FeCo LDH/NiS_x after stability testing.

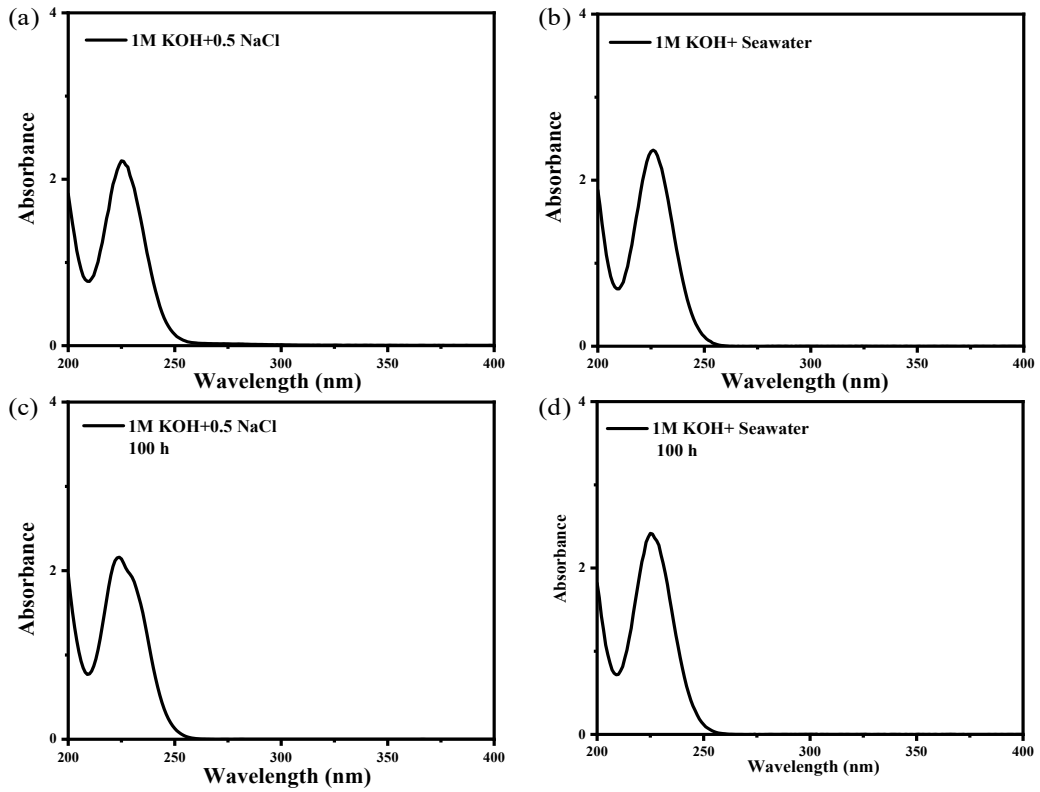

Fig. S9 UV-vis spectra of electrolytes with the addition of 0.5 M KI aqueous solutions. (a) 1.0 M KOH + 0.5 M NaCl electrolyte, (b) 1.0 M KOH +Seawater electrolyte, (c-d) Tested for 100 h under a current density of 100 mA cm^{-2} in 1.0 M KOH + 0.5 M NaCl and 1 M KOH + seawater electrolytes.

As shown in Fig. S9, the UV-vis spectra of the electrolyte after 100 hours of electrolysis is identical to that of fresh electrolyte. Furthermore, no discernible I_2 or I^{3-} signals were detected[1,2].These results therefore indicate that the Cr-FeCo LDH/NiS_x electrocatalyst maintains its high oxygen evolution reaction selectivity and chlorine resistance during prolonged operation.

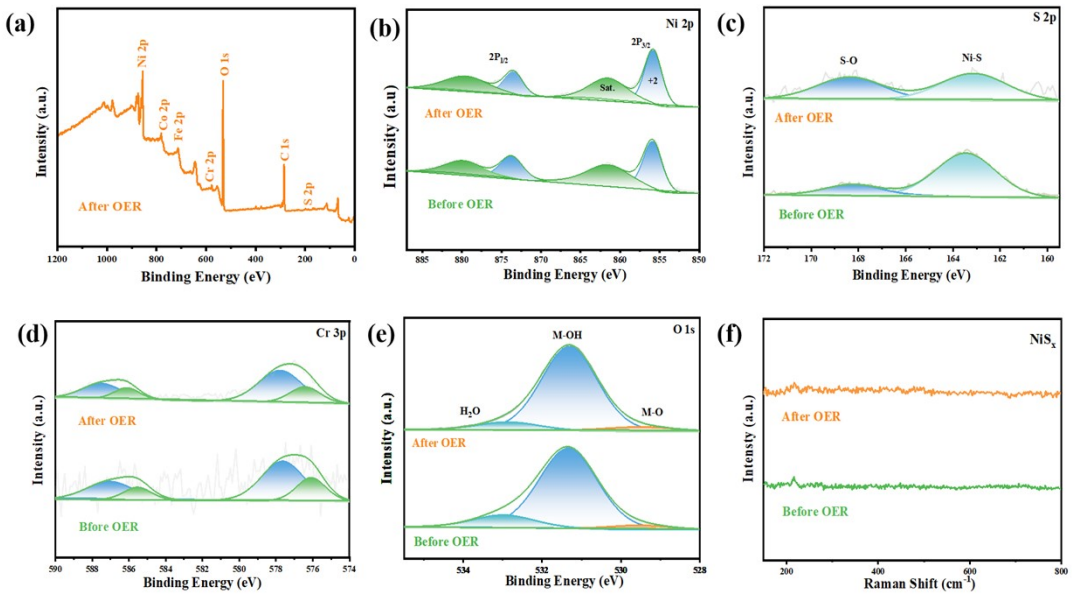

Fig. S10 (a-e) XPS survey spectra and Ni 2p, S 2p, Cr 2p, O 1s XPS spectra of Cr-FeCo LDH/NiS_x after OER, (f) Raman spectra of NiS_x before and after OER.

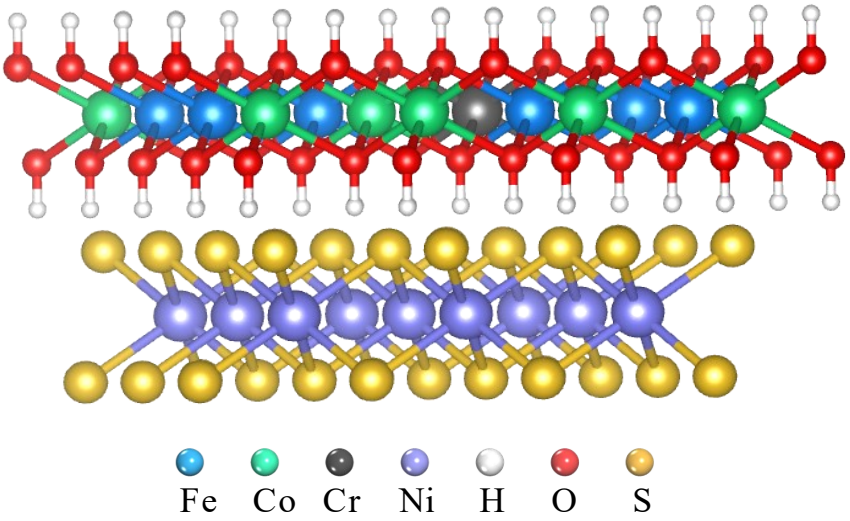

Fig. S11 Structural diagrams of Cr-FeCo LDH/NiS_x

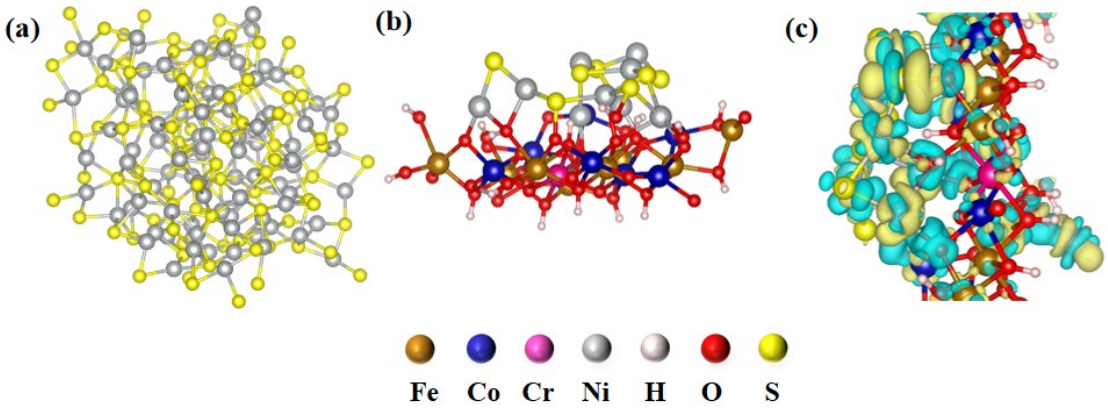

Fig. S12 (a) amorphous primitive cell phase, (b) heterojunction structure and (c) Charge density difference.

Table S1. Comparison of OER performance of Cr-FeCo LDH/$NiS_x$with the recently reported catalysts in 1 M KOH solution.

Catalyst	j / mA cm^{-2}	η / mV	Tafel slope/mV dec^{-1}	EIS/Ω	Ref.
Cr-FeCo LDH/NiS_x	10	167	45.2	0.65	This work
Cr-FeCo LDH/NiS_x	100	240	45.2	0.65	This work
S-FeOOH/$Co(OH)_2$	100	252	53.6	0.67	[3]
Cr-NiFe LDH@CuO	10	210	46.9	1.44	[4]
(NiCoFeMnCr)S	10	269	33.4	0.81	[5]
HE-LDH	10	203	53	16.17	[6]
Cr-$NiFeO_xH_y$	10	233	36.3	2.88	[7]
NiFe LDH@CoMo-P	20	236	54.4	0.46	[8]
NiOOH@FeOOH/NiOOH	10	232	46	109	[9]
Fe-NiS_2/NCNT	100	247	49	8.4	[10]
CoO@S-CoTe	100	362	56	5	[11]
FeCo LDH@Co(OH)	100	320	75.8	24	[12]
NiFe-LDH-PTA	100	223	83.28	0.40	[13]
$Ni_2Fe_1Co_{0.75}$	10/100	186/358	48.9	0.4	[14]
CoFe PBA	10	290	61.4	5.26	[15]
Cr-CoFe LDH	10	202	83	0.86	[16]
NiFe LDH/FF	10	254	51.7	0.89	[17]

Catalyst	j / mA cm^{-2}	η / mV	Tafel slope/mV dec^{-1}	EIS/Ω	Ref.
ZnCoNiFeV HELH	100	253	49	3.81	[18]
FeCo-LDH@$Co(OH)_{2-0.5}$	10	230	75.8	24	[19]

References

[1] X. Kang, F. Yang, Z. Zhang, et al., Nat. Commun. 14 (2023) 3607.

[2] R. An, G. Li, Z. Liu, Materials 17 (2024) 229

[3] Y. Zhang, W. Zhang, X. Zhang, Y. Gao, Q. Zhao, J. Li, G. Liu, Small 20 (2024) 2405080.

[4] F. Cao, M. Li, Y. Hu, X. Wu, X. Li, X. Meng, G. Qin, Chem. Eng. J. 472 (2023) 144970.

[5] L. Jiang, B. Duan, S. Lin, et al., Nano Energy 111634 (2025).

[6] D. Liu, P. Guo, X. Yan, Y. He, R. Wu, Mater. Today 80 (2024) 101–112.

[7] H. Jiao, H. Tian, C. Wang, J.-Y. Chen, Z.-Y. Zhang, P. Na, Z.-L. Wang, Appl. Catal. B: Environ. Energy 382 (2026) 125973.

[8] D. Guo, H. Xia, X. Guo, L. Wen, T. Wang, X. Li, Z. Sun, Int. J. Hydrog. Energy 79 (2024) 73-85.

[9] C. Cai, X. Huang, S. Han, et al., ACS Nano 19 (2025) 33230-33245.

[10] X. Liu, X. Zhao, S. Cao, M. Xu, Y. Wang, W. Xue, J. Li, Appl. Catal. B 331 (2023) 122715.

[11] X. Wang, Z. Mao, X. Mao, X. Hu, F. Gao, M. Gao, L. Wang, Adv. Sci. 10 (2023) 2206204.

[12] X. Yang, J. Cheng, Y. Xu, H. Li, W. Tu, J. Zhou, Chem. Eng. J. 472 (2023) 145076.

[13] J. Zhang, X. Zhang, Z. Ma, K. Fang, L. Wang, H. Ni, B. Zhao, ACS Catal. 15 (2025) 6486-6496.

[14] X. Yang, J. Liang, Q. Shi, M. J. Zachman, S. Kabir, J. Liang, G. Wu, Adv. Energy Mater. 14 (2024) 2400029.

[15] Y. Li, W. Yu, X. Chen, Int. J. Hydrog. Energy 101 (2025) 627–635.

[16] Z. Wang, W. Liu, Y. Hu, M. Guan, L. Xu, H. Li, H. Li, Appl. Catal. B 272 (2020)

118959.

[17] X. Wei, H. Xiao, Z. Zhang, P. Han, L. Wang, S. Deng, B. Jiang, Small 21 (2025) e09115.

[18] Y. Ding, Z. Wang, Z. Liang, X. Sun, Z. Sun, Y. Zhao, L. Tang, Adv. Mater. 37 (2025) 2302860.

[19] X. Yang, J. Cheng, Y. Xu, H. Li, W. Tu, J. Zhou, Chem. Eng. J. 472 (2023) 145076.